

Cite this article as: Guo Xinxin, Zhang Yongheng, Zhang Shuaifeng, et al. Numerical Analysis of Liquid Bridge Transfer in Wire Arc Additive Manufacture Process of TA31 Titanium Alloy[J]. Rare Metal Materials and Engineering, 2023, 52(05): 1643-1649.

ARTICLE

# Numerical Analysis of Liquid Bridge Transfer in Wire Arc Additive Manufacture Process of TA31 Titanium Alloy

Guo Xinxin<sup>1</sup>, Zhang Yongheng<sup>1</sup>, Zhang Shuaifeng<sup>1,2</sup>, Wei Zhengying<sup>1</sup>

<sup>1</sup> State Key Laboratory for Manufacturing Systems Engineering, Xi'an Jiaotong University, Xi'an 710049, China; <sup>2</sup> Luoyang Ship Material Research Institute, Luoyang 471039, China

**Abstract:** The three-dimensional transient computational fluid dynamics model of heat and mass transfer in the wire arc additive manufacturing (WAAM) process of TA31 titanium alloy was established. Through the volume of fluid method, the free surface was tracked. The dynamic evolution of droplet growth, liquid bridge transfer, and detachment from the wire tip into the molten pool was calculated. The velocity field of the molten pool driven by surface tension, arc pressure, arc shear, electromagnetic force, gravity, and buoyancy was calculated. The validity of the numerical model was confirmed through the results of high-speed imaging and the cross-sections of weld bead. Results show that the liquid bridge transfer mode exerts less effect on the molten pool, which is conducive to reduce the irregularity of the bead surface. With expanding the molten pool, the height of weld bead is firstly increased, then decreased, and finally becomes stable. Under the influence of arc pressure and surface tension, a crater forms on the molten pool surface, and the convection occurs inside the molten pool. The inertial force and surface tension are the most important dynamic forces in the liquid bridge transfer process, and the influence of viscosity and gravity can be neglected.

**Key words:** wire arc additive manufacturing; titanium alloy; computational fluid dynamics; molten pool; liquid bridge transfer

The Ti-6Al-3Nb-2Zr-1Mo (TA31) is a novel near- $\alpha$  titanium alloy, whose fracture toughness and welding performance are superior to those of Ti-6Al-4V alloy<sup>[1]</sup>. Thus it is suitable for operation under harsh conditions. With the development of technology and the gradual shortage of resources from land and shallow sea, the exploitation and utilization of deep sea resources are of great significance to the development of society. TA31 alloy presents a broad application prospect for the hull construction of ships and submarines and the exploitation of oil, natural gas, and other deep-sea resources<sup>[2]</sup>.

Wire arc additive manufacturing (WAAM) is considered as a cost-effective technique<sup>[3]</sup>, which is suitable for the production of large metal parts and has gained increasing popularity in recent years for the manufacture of near-net-shape and large-sized titanium alloys. However, WAAMed parts often exhibit inferior surface quality and low dimensional accuracy. The molten pool behavior can strongly affect the forming accuracy and mechanical properties of

materials<sup>[4]</sup>. Therefore, the flow and evolution of the molten pool have been extensively researched.

Zhou et al<sup>[5]</sup> established a three-dimensional transient numerical model of the tungsten inert gas (TIG) welding-WAAM process through the volume of fluid (VOF) method to track the free surface of the molten pool. Du et al<sup>[6]</sup> studied the dynamic behavior of the heat flow field and shape of molten pool caused by droplet impact during the deposition process based on the computational fluid dynamics, and investigated the influence of lateral offset distance, temperature gradient, solidification rate, and cooling rate. Ke et al<sup>[7]</sup> established a numerical model based on ultra-high frequency pulse-gas tungsten arc welding, which included force, Gaussian heat source, and droplet period transition, to simulate the five-layer deposition process. Cho et al<sup>[8]</sup> used Flow-3D software to solve the fluid flow, heat transfer, and slag particle motion models of gas metal arc welding process. These models all consider the droplet transfer process as a mass source item in the continuity equation, and assume that the mass input

Received date: September 23, 2022

Foundation item: Applied Innovation Project

Corresponding author: Wei Zhengying, Ph. D., Professor, State Key Laboratory for Manufacturing Systems Engineering, Xi'an Jiaotong University, Xi'an 710049, P. R. China, E-mail: zywei@xjtu.edu.cn

Copyright © 2023, Northwest Institute for Nonferrous Metal Research. Published by Science Press. All rights reserved.

position is a spherical area and the droplet enters the molten pool through the spherical impact mode. However, the liquid bridge transfer mode is not considered.

Combining the rigid body motion of the wire feeding process, the numerical simulation can better represent the actual manufacture process and investigate the behavior of liquid bridge flow in the laser wire deposition additive manufacturing process<sup>[9-11]</sup>. Chen et al<sup>[12]</sup> developed a three-dimensional wire feeding model based on hybrid theory and the Euler method to study the transient coupling behavior of heat and mass transfer in the plasma arc WAAM process. Three different metal transfer modes have been discussed under different wire feeding speeds: spherical droplet mode, droplet-liquid bridge mode, and solid-liquid bridge mode. However, these models are complex and require more computational cost. Zhao et al<sup>[13]</sup> established a model to simulate the growth process of the droplet at the end of the welding wire. The droplet is subject to gravity, buoyancy, surface tension, Marangoni force, and electromagnetic force. The wire feeding process is simplified as the flow of a high-temperature liquid from a virtual pipe. But the liquid bridge transfer has rarely been studied.

In this research, a simplified model was established to simulate the liquid bridge transfer during WAAM process. The melting process of the wire was considered as a flow of molten metal from the wire end into the molten pool for simplification. Then, the metal liquid bridge transfer and the molten pool behavior of the TA31 titanium alloy during WAAM process were analyzed.

## 1 Experiment

TIG welding-WAAM system was used. The torch head was perpendicular to the horizontal substrate and the inclination angle of the wire was set as 22°. The welding current was 160 A, the travel speed was 120 mm/min, and the wire feeding speed was 800 mm/min. A drag-type oxidation shield was installed behind the torch nozzle to provide local protection during the cooling process. Under the flow rate of 30 L/min, the bead surface showed no signs of oxidation. Argon was

employed as the protective gas for the torch and the protective cover. The raw material of substrate and wire was TA31 alloy, whose chemical composition is shown in Table 1. The surface was polished by sandpaper to remove contaminants. The deposition process was monitored by Xiris XVC-1100 welding camera with the image acquisition frequency of 50 Hz. The cross-section morphologies of the deposited bead were obtained through electrical discharge machining, grinding, polishing, and etching by etchant (5vol% HNO<sub>3</sub>, 10vol% HF, and 85vol% H<sub>2</sub>O) for 5–10 s.

## 2 Numerical Modelling

In this research, the VOF model was established based on the external environment and the molten pool. The computational domain was 30 mm×10 mm×10 mm, and the gas domain height was 2 mm. The symmetry of WAAM was considered for simplification, and only half of the deposition region was modeled. The mesh size was 0.2 mm, which could accurately describe the free surface and droplet impact of the molten pool<sup>[6,14]</sup>. The model considered the controlling factors of molten pool fluid flow, including the volume forces (gravity, buoyancy, electromagnetic force) and surface forces (surface tension, arc pressure, arc shear stress), as shown in Fig.1.

### 2.1 Governing equation

In the computational domain, the model considered the liquid metal as an incompressible Newtonian fluid with laminar flow. The buoyancy caused by the density difference through Boussinesq approximation was considered, and the evaporation-related mass loss was neglected. The partial differential equations to solve the mass, momentum, and energy conservation equations can be expressed by Eq.(1–3), respectively:

$$\nabla \cdot (\rho \mathbf{v}) = m_s \quad (1)$$

$$\rho \left( \frac{\partial \mathbf{v}}{\partial t} + \mathbf{v} \cdot \nabla \mathbf{v} \right) - \mu \nabla^2 \mathbf{v} = -\nabla P + S_F \quad (2)$$

$$\rho \left( \frac{\partial H}{\partial t} + \mathbf{v} \cdot \nabla H \right) - \nabla \cdot (k \nabla T) = S_E \quad (3)$$

where  $m_s$  represents the increase in mass due to metal transfer;

Table 1 Chemical composition of TA31 alloy (wt%)

Al	Nb	Zr	Mo	Fe	Si	C	N	H	O	Ti
5.5–6.5	2.5–3.5	1.5–2.5	0.6–1.5	≤0.25	≤0.15	≤0.10	≤0.05	≤0.015	≤0.15	Bal.

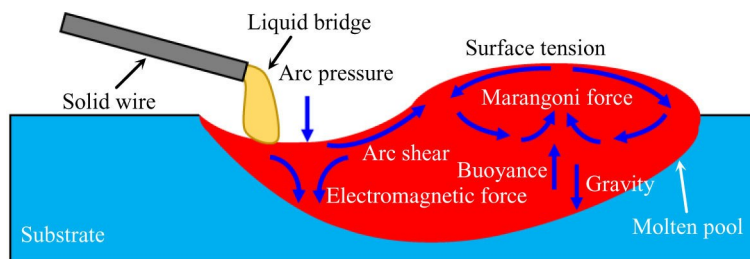


Fig.1 Schematic diagram of driving forces on molten pool

$\rho$  is the density;  $\mathbf{v}$  is the velocity vector;  $t$  is time;  $\mu$  is viscosity;  $P$  is pressure;  $S_f$  represents the momentum source term (gravity, buoyancy, velocity decay in mushy zone, electromagnetic force, arc pressure, arc shear force, and surface tension);  $H$  is enthalpy;  $k$  is the thermal conductivity;  $T$  is temperature;  $S_e$  is the energy source term.

## 2.2 Driving force

The electromagnetic force  $F_e$  could be represented by Eq.(4), as follows:

$$\mathbf{F}_e = \mathbf{J} \times \mathbf{B} \quad (4)$$

where  $\mathbf{J}$  denotes the electric current density, and  $\mathbf{B}$  denotes the magnetic induction intensity.

Assuming that the surface current density of the molten pool obeys the Gaussian distribution, the components of the electromagnetic force along  $x$ ,  $y$ , and  $z$  directions could be expressed by Eq.(5-7), respectively:

$$(\mathbf{J} \times \mathbf{B})_x = -\frac{\mu_0 I^2}{4\pi^2 \sigma_j^2 r} \exp\left(-\frac{r^2}{2\sigma_j^2}\right) \times \left[1 - \exp\left(-\frac{r^2}{2\sigma_j^2}\right)\right] \left(1 - \frac{z}{L}\right)^2 \frac{(x - x_0 - vt)}{r} \quad (5)$$

$$(\mathbf{J} \times \mathbf{B})_y = -\frac{\mu_0 I^2}{4\pi^2 \sigma_j^2 r} \exp\left(-\frac{r^2}{2\sigma_j^2}\right) \times \left[1 - \exp\left(-\frac{r^2}{2\sigma_j^2}\right)\right] \left(1 - \frac{z}{L}\right)^2 \frac{y}{r} \quad (6)$$

$$(\mathbf{J} \times \mathbf{B})_z = -\frac{\mu_0 I^2}{4\pi^2 \sigma_j^2 r} \exp\left(-\frac{r^2}{2\sigma_j^2}\right) \left(1 - \frac{z}{L}\right) \quad (7)$$

where  $\mu_0$  is the magnetic permeability,  $I$  is the current,  $\sigma_j$  is the current density distribution parameter,  $r$  is the distance from a point to the center of the welding torch,  $L$  is the substrate thickness,  $x$  is the position along  $x$  axis,  $x_0$  is the initial position along  $x$  axis,  $y$  is the position along  $y$  axis, and  $z$  is the position along  $z$  axis.

Surface tension was the force produced by the mutual attraction of the molecules in the fluid, as follows:

$$\mathbf{F}_{st} = -\gamma \nabla \cdot \hat{\mathbf{n}} \quad (8)$$

$$\hat{\mathbf{n}} = \frac{\nabla \alpha}{\|\nabla \alpha\|} \quad (9)$$

where  $\gamma$  is the surface tension coefficient,  $\hat{\mathbf{n}}$  is the vector normal to the local free surface, and  $\alpha$  is the volume fraction function of fluid.

The Marangoni force  $F_{Ma}$  was caused by the gradient of surface tension, which promoted the convection of liquid metal in the pool and could be expressed, as follows:

$$\mathbf{F}_{Ma} = \frac{\partial \gamma}{\partial T} \frac{\partial T}{\partial s} \quad (10)$$

where  $s$  represents the local tangent vector of the free surface.

The presence of the arc plasma caused the pressure on the surface of molten pool. Assuming that the arc pressure obeys the Gaussian distribution, the arc pressure could be expressed, as follows:

$$\mathbf{F}_{arc} = P_{max} \exp\left(-\frac{r^2}{2\sigma_p^2}\right) \quad (11)$$

where  $\sigma_p$  denotes the parameter of arc pressure distribution and  $P_{max}$  is the maximum pressure.

The arc shear stress  $F_\tau$  resulted from the difference in velocity between the arc plasma and the fusion pool, which increased rapidly from the arc center and then decreased, as follows:

$$\mathbf{F}_\tau = 0.069 I^{1.5} g_a(r) \hat{\mathbf{t}} \quad (12)$$

$$g_a(r) = \begin{cases} a_{g1} r^3 + a_{g2} r^2 + a_{g3} r + a_{g4} & r \leq 1.53 \text{ mm} \\ a_{g5} \exp\left(-\frac{r}{a_{g6}}\right) + a_{g7} & r > 1.53 \text{ mm} \end{cases} \quad (13)$$

$$\hat{\mathbf{t}} = \frac{\mathbf{r} - \hat{\mathbf{n}}(\mathbf{r} \cdot \hat{\mathbf{n}})}{\|\mathbf{r} - \hat{\mathbf{n}}(\mathbf{r} \cdot \hat{\mathbf{n}})\|} \quad (14)$$

where  $g_a(r)$  is the distribution function of arc shear stress (0-1);  $a_{g1}$ - $a_{g6}$  are related parameters<sup>[15]</sup>;  $\mathbf{r}$  is the radial vector in the  $xy$  plane.

## 2.3 Arc heat source model

A double ellipsoid heat source distribution model was employed to depict the distribution of the arc heat source, as follows:

$$q_{arc}(x,y,z) = \begin{cases} \frac{6\sqrt{3} f_r \eta UI}{a_r b c \pi \sqrt{\pi}} \exp\left[-\frac{3(x-vt)^2}{a_r^2}\right] \left[-\frac{3y^2}{b^2} - \frac{3z^2}{c^2}\right] & x \geq vt \\ \frac{6\sqrt{3} f_r \eta UI}{a_r b c \pi \sqrt{\pi}} \exp\left[-\frac{3(x-vt)^2}{a_r^2}\right] \left[-\frac{3y^2}{b^2} - \frac{3z^2}{c^2}\right] & x < vt \end{cases} \quad (15)$$

where  $U$  is the voltage;  $\eta$  is the arc efficiency;  $f_f$  and  $f_r$  denote the heat distribution coefficients of the front and rear semi-ellipsoids, respectively ( $f_f + f_r = 2$ ); the parameters  $a_r$ ,  $a_r$ ,  $b$ , and  $c$  describe the heat flow distribution of the volumetric heat source.

## 2.4 Boundary condition

The heat loss  $q_{loss}$  caused by the convection and radiation in the model could be expressed, as follows:

$$q_{loss} = -[h_c(T - T_{ref}) + \sigma \varepsilon(T^4 - T_{ref}^4)] \quad (16)$$

where  $h_c$  is the thermal convection coefficient,  $T_{ref}$  is the ambient temperature,  $\sigma$  is the Stefan-Boltzmann constant, and  $\varepsilon$  is the radiation emissivity.

The droplet was generated from the wire tip at a certain temperature and transition frequency, as follows:

$$v_w \Delta t = v_{drop} \Delta t_{inlet} \quad (17)$$

where  $\Delta t$  is the droplet transition period with  $\Delta t = 203$  ms;  $v_w$  is the wire feeding speed;  $v_{drop}$  is the droplet falling speed;  $\Delta t_{inlet}$  is the droplet falling time.

The governing equations and associated physical models could be solved by FLUENT CFD software. The material parameters related to the models are displayed in Table 2. The time step was  $1 \times 10^{-4}$  s, and a simulation of 10 s required computation of approximately 96 h through the Intel i9-10980XE CPU processor.

**Table 2** Thermo-physical properties of TA31 alloy

Parameter	Value
Density/kg·m <sup>-3</sup>	4490
Specific heat of the solid phase/J·kg <sup>-1</sup> ·K <sup>-1</sup>	690
Specific heat of the liquid phase/J·kg <sup>-1</sup> ·K <sup>-1</sup>	960
Thermal conductivity of the solid phase/W·m <sup>-1</sup> ·K <sup>-1</sup>	23
Thermal conductivity of the liquid phase/W·m <sup>-1</sup> ·K <sup>-1</sup>	30
Dynamic viscosity/kg·m <sup>-1</sup> ·s <sup>-1</sup>	0.0026
Surface tension coefficient at liquidus temperature/N·m <sup>-1</sup>	1.6
Temperature coefficient of surface tension/N·m <sup>-1</sup> ·K <sup>-1</sup>	-2.4×10 <sup>-4</sup>
Thermal expansion coefficient/K <sup>-1</sup>	1.2×10 <sup>-5</sup>
Solidus temperature/K	1893
Liquidus temperature/K	2009
Latent heat of melting/J·kg <sup>-1</sup>	3.2×10 <sup>5</sup>

### 3 Results and Discussion

#### 3.1 Liquid bridge transfer behavior

Fig. 2 shows the experimental and simulated liquid bridge generation and metal transfer process, which includes three stages: droplet growth, liquid bridge transition, and detachment from the wire. The red area in the simulation results represents the molten pool, indicating that the temperature exceeds the liquidus temperature of TA31 alloy.

Fig. 2a and 2d show the beginning of the metal transfer process. The wire is heated through arc melting. The droplet at

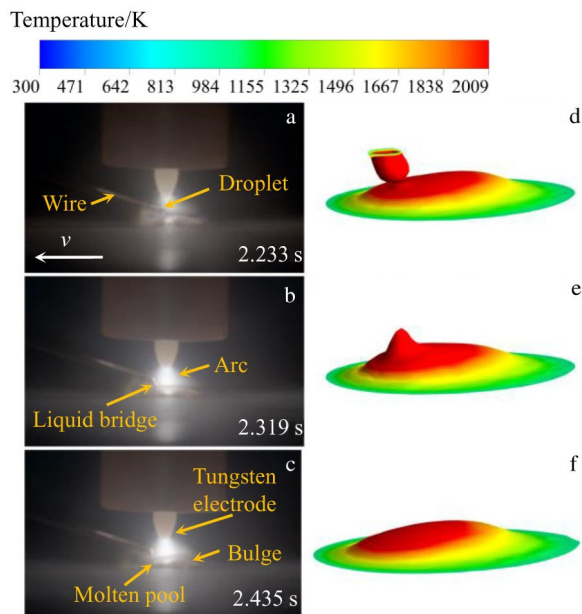


Fig. 2 Experimental (a–c) and simulated (d–f) liquid bridge behavior of TA31 alloy during metal transfer: (a, d) droplet growth stage, (b, e) liquid bridge transition stage, and (c, f) detachment stage

the wire end retains its spherical shape as a result of surface tension resistance. When the droplet grows to a certain extent, due to the short distance between the wire end and the molten pool, the droplet contacts the molten pool before complete growth. Because of the electromagnetic force, gravity, and arc pressure, the droplet is stretched, and the high surface tension and viscosity of the melted titanium alloy result in the continuous fluid during transfer process<sup>[16]</sup>. As shown in Fig. 2b and 2e, when the melted alloy is in contact with the molten pool, the melted alloy flows from the wire end to the molten pool through the liquid bridge. Then, the fluid in the molten pool flows to the rear and sides. Compared with the spherical droplet transition mode, the liquid bridge mode requires less mass and less momentum when the droplet enters the molten pool, leading to less impact on the fluctuation of molten pool<sup>[17]</sup>. The metal transfer process is more stable under this mode, presenting better geometric accuracy and reduced surface irregularity. Finally, the droplet detaches from the wire and completely merges into the molten pool, as shown in Fig. 2c and 2f. The whole process is regarded as a metal transfer cycle.

After the liquid bridge falls off, the molten alloy driven by the arc pressure, electromagnetic force, Marangoni force, surface tension, and inertial force flows to the back-end of the molten pool, forming a bulge. With decreasing the heat input, i. e., when the heat source gradually moves away, the accumulated molten metal begins to cool and solidify. Fig. 3 shows the evolution morphology of the deposited bead during WAAM process. In the initial stage, the length of the molten pool is continuously increased due to the heat accumulation along  $x$  direction<sup>[18]</sup>. With the deposition proceeding, the temperature distribution becomes stable, leading to a relatively stable shape of the molten pool.

Fig. 4a shows the bead morphology after WAAM process. Fig. 4b shows the numerical simulation and the experiment results of cross-section of the deposition morphologies after WAAM process. The height of the alloy accumulation is approximately 1.4 mm, and the width is approximately 6 mm. The simulation results fit well with the experiment results, which indicates that the computational fluid dynamics model can effectively simulate the metal transfer process and molten pool behavior during WAAM process.

#### 3.2 Molten pool flow behavior

The complex flow pattern in the molten pool results from several driving forces, including the droplet transfer, surface tension, arc pressure, arc shear force, electromagnetic force, gravity, and thermal buoyancy. At the initial stage of the liquid bridge transition, the momentum is transmitted to the molten pool and reaches the highest velocity when the droplet touches the molten pool. The wire feeding has an angle, which results in a flow velocity perpendicular to the tangent line between the pool and the droplet. The velocity is approximately 1 m/s, as seen in Fig. 5a. However, the velocity of melted alloy decreases rapidly after entering the molten pool, which has little impact on the surface of molten pool. The melted alloy is spread towards the back side of the molten pool due to the

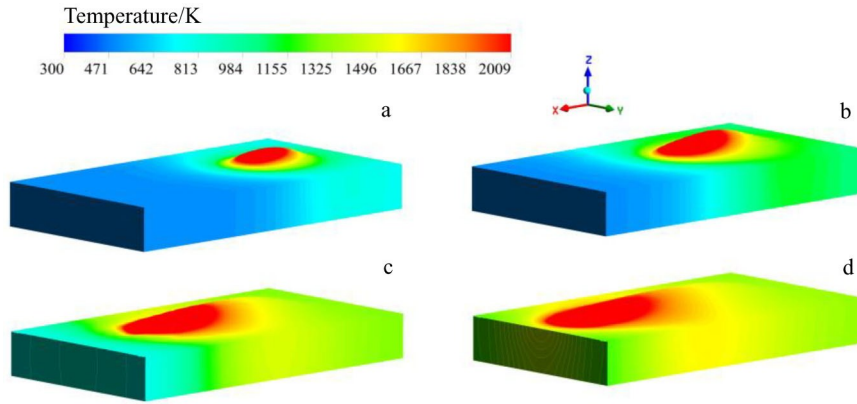


Fig.3 Simulated deposition morphologies during WAAM process: (a)  $t=2$  s; (b)  $t=4$  s; (c)  $t=8$  s; (d)  $t=10$  s

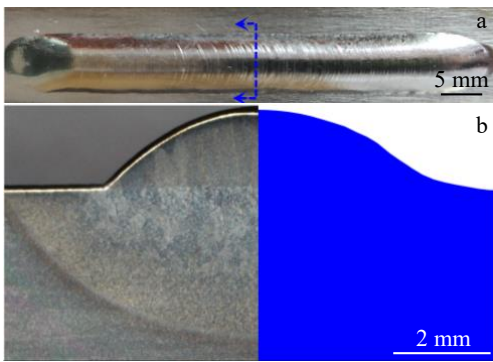


Fig.4 Appearance of deposition after WAAM process (a); comparison of experimental and simulated cross-sections after WAAM process (b)

influence of inertial force and surface tension<sup>[9]</sup>, forming a clockwise eddy along the fusion line (Fig.5b).

Under the influence of the induced magnetic field, the melted alloy on the molten pool surface tends to flow downward, resulting in more heat load on the bottom. The solid substrate below the solid-liquid interface is further melted, resulting in a deeper molten pool. Once the molten pool reaches a relatively stable state, the surface tension is decreased with increasing the temperature due to the negative temperature gradient of the surface tension coefficient. The melted alloy in the molten pool then flows from the inner side to the outer side, transferring the heat caused by arc from the center to the edge of the molten pool (thermal convection), leading to the expansion of molten pool<sup>[19]</sup>.

According to Fig.5c and 5d, it is clear that the molten pool at initial stage is smaller. With the deposition process proceeding, the aggregation of melted alloy is enhanced on the substrate, leading to the expansion of molten pool. Meanwhile, due to the sufficient diffusion of melted alloy, the bulge height is decreased, and the heat convection is also enhanced. The crater on the molten pool surface (Fig. 5d) results from the combined effects of arc pressure and surface tension. In the center of molten pool, the arc pressure is in the dominant position; around the molten pool, the surface tension

is in the dominant position. Therefore, the melted alloy in the center flows outward and forms an arc-shaped crater<sup>[5]</sup>.

### 3.3 Dimensionless number

The fluid dynamics during the liquid bridge transition was investigated through the dimensionless numbers for quantitative analysis.

Péclet number ( $Pe$ ) indicates the relative importance of convective heat transfer over conductive heat transfer, and it is used to assess the importance of convection in molten metals, as follows:

$$Pe = \frac{LU}{k/\rho c_p} \quad (18)$$

where  $c_p$  is the specific heat capacity of the fluid;  $k$  is the thermal conductivity;  $U$  is the characteristic velocity (maximum velocity within the molten pool<sup>[20]</sup>);  $L$  is the characteristic length.

Weber number ( $We$ ) can evaluate the relative importance of fluid inertia over surface tension, as follows:

$$We = \frac{\rho LU^2}{\gamma} \quad (19)$$

Reynolds number ( $Re$ ) describes the relative magnitude between the inertia force and viscous force, and defines the dissipating rate of liquid bridge inertia caused by viscous force, as follows:

$$Re = \frac{\rho UL}{\mu} \quad (20)$$

Bond number ( $Bo$ ) measures the importance of gravity and surface tension on the flow of liquid, as follows:

$$Bo = \frac{\rho g L^2 U}{\gamma} \quad (21)$$

Froude number ( $Fr$ ) can characterize the relative magnitude between fluid inertia force and gravity, as follows:

$$Fr = \frac{U}{\sqrt{gL}} \quad (22)$$

Capillary number ( $Ca$ ) represents the ratio of viscous force to surface tension, as follows:

$$Ca = \frac{\mu U}{\gamma} \quad (23)$$

The calculated  $Pe$  number in this research is significantly

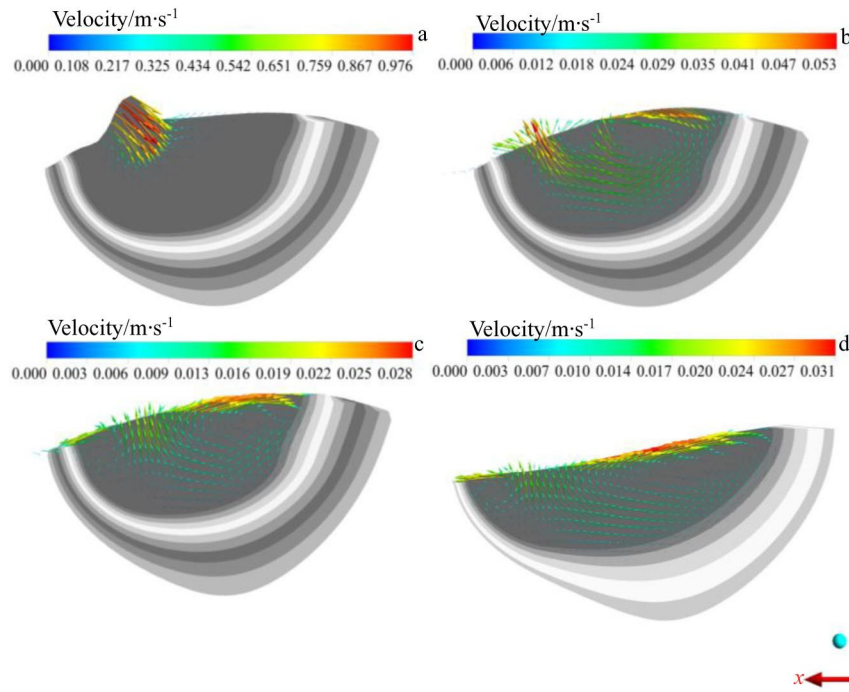


Fig.5 Flow behavior of molten pool during WAAM process: (a)  $t=2.319$  s; (b)  $t=2.324$  s; (c)  $t=2.435$  s; (d)  $t=7.104$  s

larger than 1, which indicates that the influence of molten metal convection is significant<sup>[21]</sup>, as shown in Table 3. The calculation results reveal that the convective heat transfer is the primary mechanism of heat transfer in the liquid bridge transfer process. The  $We$  and  $Re$  values are both greater than 1, indicating that the inertia force is the dominant driving force affecting the flow in the liquid bridge process<sup>[22]</sup>. The  $Re$  value has the magnitude of  $10^3$ , suggesting that the flow around the liquid bridge is laminar<sup>[23]</sup>. The  $Bo$  and  $Fr$  values show that the effect of gravity is less significant<sup>[19,24]</sup>. The calculated  $We$  value is only 3.368, which can be attributed to several factors. The slow wire feeding speed, the small distance, the small tilt angle between the wire and substrate, and the large liquid bridge diameter are all conducive to decrease the inertia and to enhance the surface tension effect, which improves the forming accuracy. Furthermore, the calculated  $Ca$  value is relatively small, indicating that the role of viscous force in

fluid flow is negligible, compared to surface tension<sup>[25]</sup>.

## 4 Conclusions

1) Due to the short distance between the wire end and the molten pool, the droplet does not have enough space to fully grow. When the droplet comes into contact with the molten pool, the melted TA31 alloy flows from the wire end to the molten pool through liquid bridge, which results in a small impact on the molten pool and improves the surface quality of the deposition.

2) During the initial stage of wire arc additive manufacturing (WAAM) process, the size of the molten pool is small. With the deposition proceeding, the aggregation of melted alloy is increased on the substrate, leading to the expansion of molten pool. Meanwhile, due to the sufficient diffusion of the melted alloy, the bulge height is decreased, and the heat convection is enhanced.

3) When the depth/width of molten pool and the deposition height become stable, a crater forms on the molten pool surface and the convective eddies appear in the molten pool due to the arc pressure and surface tension.

4) Inertia force and surface tension are the most important driving forces to influence the flow behavior of liquid bridge, whereas the effect of viscosity and gravity can be neglected. The small Weber number of the liquid bridge is favorable to obtain cladding layers with good surface smoothness and dimensional accuracy.

Table 3 Dimensionless numbers in liquid bridge transfer process

Dimensionless parameter	Value
Péclet number, $Pe$	$1.724 \times 10^2$
Weber number, $We$	3.368
Reynolds number, $Re$	$2.072 \times 10^3$
Bond number, $Bo$	$3.961 \times 10^{-2}$
Froude number, $Fr$	9.221
Capillary number, $Ca$	$1.625 \times 10^{-3}$

## References

- 1 Ren J Q, Qi W, Zhang B B et al. *Materials Science and*

- Engineering A*[J], 2022, 831: 142 187
- 2 Li X Q, Wang L W, Fan L et al. *Journal of Materials Research and Technology*[J], 2022, 17: 374
  - 3 Li Quan, Wang Guoqing, Dong Mingye et al. *Rare Metal Materials and Engineering*[J], 2021, 50(5): 1649 (in Chinese)
  - 4 Aucott L, Dong H B, Mirihanage W et al. *Nature Communications*[J], 2018, 9(1): 5414
  - 5 Zhou Xiangman, Wang Boyun, Yuan Youlu et al. *Journal of Mechanical Engineering*[J], 2022, 58(10): 103 (in Chinese)
  - 6 Du J, Zhang Y H, Wei Z Y et al. *Additive Manufacturing*[J], 2022, 58: 103 039
  - 7 Ke W C, Oliveira J P, Cong B Q et al. *Additive Manufacturing*[J], 2022, 50: 102 513
  - 8 Cho D W, Park Y D, Cheepu M. *International Communications in Heat and Mass Transfer*[J], 2021, 125: 105 243
  - 9 Hu R Z, Luo M L L, Liu T T et al. *Science and Technology of Welding and Joining*[J], 2019, 24(5): 401
  - 10 Liang L J, Hu R Z, Wang J S et al. *Journal of Manufacturing Processes*[J], 2021, 69: 602
  - 11 Noori R A S M A, Hagqvist P, Sikström F et al. *Frontiers in Space Technologies*[J], 2022, 3: 880 012
  - 12 Chen X, Wang C, Ding J L et al. *Journal of Manufacturing Processes*[J], 2022, 83: 300
  - 13 Zhao W Y, Wei Y H, Long J W et al. *Welding in the World*[J], 2021, 65(8): 1571
  - 14 Ji F L, Qin X P, Hu Z Q et al. *International Communications in Heat and Mass Transfer*[J], 2022, 130: 105 789
  - 15 Meng X M, Qin G L, Bai X Y et al. *Journal of Materials Processing Technology*[J], 2016, 236: 225
  - 16 Zhou S Y, Xie H, Ni J Q et al. *Journal of Manufacturing Processes*[J], 2022, 82: 159
  - 17 Huang J K, Li Z X, Yu S R et al. *Welding in the World*[J], 2022, 66(3): 481
  - 18 Fan H G, Kovacevic R. *Proceedings of the Institution of Mechanical Engineers, Part B: Journal of Engineering Manufacture*[J], 2006, 220(7): 1107
  - 19 Wang Xinxin, Fan Ding, Huang Jiankang et al. *Journal of Mechanical Engineering*[J], 2015, 51(10): 69 (in Chinese)
  - 20 Ou W, Mukherjee T, Knapp G L et al. *International Journal of Heat and Mass Transfer*[J], 2018, 127(Part C): 1084
  - 21 Wei H L, Mukherjee T, Zhang W et al. *Progress in Materials Science*[J], 2021, 116: 100 703
  - 22 Chen M Z, Lu Y, Wang Z D et al. *Optics & Laser Technology*[J], 2021, 136: 106 745
  - 23 Kumar A, Roy S. *International Journal of Thermal Sciences*[J], 2010, 49(2): 397
  - 24 Cao L. *Computational Materials Science*[J], 2020, 179: 109 686
  - 25 Xu G X, Li P F, Cao Q N et al. *Optics & Laser Technology*[J], 2018, 100: 244

## TA31 钛合金电弧增材制造过程液桥过渡数值分析

郭鑫鑫<sup>1</sup>, 张永恒<sup>1</sup>, 张帅锋<sup>1,2</sup>, 魏正英<sup>1</sup>

(1. 西安交通大学 机械制造系统工程国家重点实验室, 陕西 西安 710049)

(2. 中国船舶集团有限公司第七二五研究所, 河南 洛阳 471039)

**摘要:** 建立了电弧熔丝增材制备 TA31 钛合金过程传热传质的三维瞬态计算流体力学模型, 采用流体体积法对自由表面进行追踪, 计算了熔滴生长、液桥过渡和脱离焊丝进入熔池的动态演化, 以及在表面张力、电弧压力、电弧剪切力、电磁力、重力和热浮力的作用下熔池流体流动的速度分布, 并通过与高速成像以及沉积层横截面的比较, 验证了该数值模型的有效性。结果表明: 液桥过渡模式对熔池冲击较小, 有利于减少成形表面的不规则性。随着熔池几何形状的扩大, 沉积层高度先增大后减小, 最后趋于稳定。在电弧压力和表面张力的作用下, 熔池表面形成凹陷, 熔池内部产生对流。惯性力和表面张力是影响液桥流动的最重要驱动力, 粘性力和重力的影响可以忽略不计。

**关键词:** 电弧增材制造; 钛合金; 计算流体力学; 熔池; 液桥过渡

作者简介: 郭鑫鑫, 男, 1995 年生, 博士生, 西安交通大学机械制造系统工程国家重点实验室, 陕西 西安 710049, E-mail: guo\_ustb@163.com